Rare Metal Materials and Engineering
Volume 55, Issue 5, May 2026
Available online at www.rmme.ac.cn

Science Press

Cite this article as: Zhang Limin, Zhang Hongju, Xia Wen, et al. Real-Time Tracking of Tensile Deformation Behavior in GH4169 Under Tensile Stress Based on DIC and EBSD[J]. Rare Metal Materials and Engineering, 2026, 55(05): 1199-1208. DOI: https://doi.org/10.12442/j.issn.1002-185X.20250350.

ARTICLE

Real-Time Tracking of Tensile Deformation Behavior in GH4169 Under Tensile Stress Based on DIC and EBSD

Zhang Limin, Zhang Hongju, Xia Wen, Yu Limin, Cao Dongdong, Jia Rongguang

Guobiao (Beijing) Testing & Certification Co., Ltd, Beijing 101400, China

Abstract: The deformation behavior of GH4169 superalloy under room-temperature uniaxial tension was investigated through synchronized mesoscopic digital image correlation (DIC) and electron backscatter diffraction (EBSD) in-situ characterization techniques. Results show that in the field of grain deflection dynamics, through quantitative analysis using the independently developed M-DIC software, during uniaxial tension with significant bidirectional rotation along the tensile axis and the stress level of 1100 MPa, oscillatory rotation of ±0.6° can be obtained, and microvoids are generated at the grain boundaries with 45° to the stress axis. EBSD crystallographic analysis demonstrates the load-dependent slip system evolution: in the initial stage, the soft-oriented systems with high Schmid factor (>0.4) is activated and then transformed into hard-oriented systems during cross-slip, generating parallel slip bands and dislocation pile-ups at grain boundaries. During the uniaxial tensile process, the characteristic of strain energy accumulation is observed, which follows a two-stage accumulation pattern: initial grain boundary localization (Stage I) and intragranular propagation (Stage II). Ultimately, the intergranular cracks are initiated at triple junctions, and the twin boundaries exhibit superior mechanical stability compared with the large-angle grain boundaries. Deformation texture characteristics indicate the copper-type components, including C{112}<11$\bar{1}$>, S{123}<63$\bar{4}$>, and B{110}<1$\bar{1}$0>. The complete deformation sequence is as follows: cross-slip of soft-oriented slip systems→initiation of dislocation slip→strain partitioning through grain rotation→intergranular stress concentration→damage dominated by boundary cracking. The cross-scale deformation mechanism revealed in this study provides critical guidance for the crystal boundary engineering to optimize nickel-based superalloys.

Key words: GH4169; in-situ tension; grain rotation; slip; texture

1 Introduction

Nickel-based superalloys have become critical materials across multiple fields under extreme environments, owing to their exceptional high-temperature strength, creep resistance, and corrosion resistance. Because of its exceptional mechanical properties, GH4169 superalloy is commonly used in nuclear reactors, turbocharger rotors, land-based gas turbine engines, and aeronautical gas turbine engines[1–2]. The deformation behavior of this advanced material has garnered significant research attention, particularly the microscopic damage initiation under mechanical loading. It has been demonstrated that localized slip band formation within individual grains (precursors to crack nucleation) occurs under both monotonic and cyclic straining states[3–5]. Deng et al[6] conducted a study on the microstructure of GH4169 superalloy under temperature/stress coupling conditions. Post-aging, coarsening, and reducing content of γ'' phase in GH4169 superalloy lead to inferior tensile strength and yield strength. Besides, the stress required for microcrack formation is decreased with the increase in δ phase size. Sliding dislocations readily bypass the coarse γ'' precipitates or traverse the γ''-deficient regions, propagating toward newly formed microcracks and accelerating their growth. Concurrently, coordinated grain group movements through rotational accommodation mechanisms significantly influence the macroscopic mechanical responses[7]. These phenomena underscore the fundamental connection between microstructural evolution and material performance.

Contemporary research approaches predominantly consider

Received date: July 01, 2025
Foundation item: National Natural Science Foundation of China (2022YFF0609300)
Corresponding author: Zhang Hongju, Master, Professor, Guobiao (Beijing) Testing & Certification Co., Ltd, Beijing 101400, P. R. China, Tel: 0086-10-82241376, E-mail: zhanghongju@gbtcgroup.com

two distinct scales. One is microscale analysis, which focuses on intracrystalline phenomena (dislocation dynamics and precipitate interactions) but often yields localized conclusions with restricted macroscopic relevance[8]. The other is macroscale investigations, which emphasize processing-property relationships (thermomechanical treatments and defect engineering) while neglecting intrinsic microstructural interactions[9]. Those researches create a critical knowledge gap to understand mesoscale mechanisms that govern the grain group behavior during plastic deformation. Zhu et al[10] proposed a rotational vortex model, suggesting that material failure is initiated when the translational-rotational equilibrium within grain assemblies becomes disrupted. This theory posits that the macroscopic mechanical properties inherently derive from collective grain group resistance to deformation vortices. Nevertheless, experimental validation requires synchronous quantification of grain rotation kinematics and intragranular slip activities across multiple scales. Shen et al[11] investigated the effects of variable-amplitude loading on the very-high-cycle-fatigue behavior of IN718 superalloy under high-temperature conditions. It provides a comprehensive exploration encompassing both macroscale mechanical characterization and microscale analysis of microcrack initiation and propagation. Zhao et al[12] integrated multiscale characterization data with mechanistic analysis, demonstrating a comprehensive approach to correlate material behavior with underlying principles.

Digital image correlation (DIC) technique enables precise measurement of full-field strain with 0.01 pixel resolution[13–19]. Combining DIC with in-situ electron backscattered diffraction (EBSD) technique[20–21] that is capable of resolving real-time microstructural evolution under load, this approach provides novel insights into deformation mechanisms[22–23]. The room-temperature tensile behavior of GH4169 superalloy was investigated through this DIC+in-situ EBSD method. Synchronized analyses were conducted, including mesoscopic grain rotation via custom M-DIC software, crystallographic slip system evolution through EBSD, and micromechanical strain-partitioning patterns. A multiscale framework correlating grain boundary kinematics with intragranular dislocation dynamics was established. This research provides theoretical guidance for advanced superalloy development.

2 Experiment

This research used solid-solution-aged GH4169 superalloy extracted from hot-rolled plates. Two dog-bone shaped tensile specimens with continuous transitional geometry were fabricated via wire electrical discharge machining along the rolling direction with dimensional accuracy of ±5 μm. Fig. 1 shows the schematic diagram of tensile specimen for in-situ DIC test. The double-hinged sheet tensile specimen design ensured the precise coaxial alignment between clamping zones and gauge section.

The specimen plane (transverse direction-loading direction) was polished with 120#, 500#, 1200#, and 2400# SiC paper in sequence, and the final mirror finish was operated with colloidal silica suspension of 0.05 μm in size. The final specimen thickness was 0.99±0.03 mm.

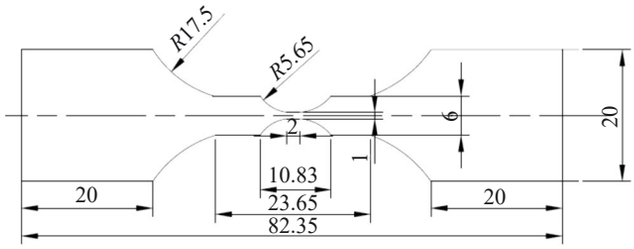

Fig.1 Schematic diagram of tensile specimen for in-situ DIC test

DIC specimens were then treated with metallographic etching by immersing in modified Marble reagent (20 mL HCl+20 mL C_2H_5OH+1.5 g $CuSO_4 \cdot 5H_2O$) for 60 s. Specimens for EBSD analysis underwent electrolytic polishing treatment: immersing in chilled (− 30 ℃) 10vol% $HClO_4$+90vol% CH_3CH_2OH solution. The treatment parameters were direct current of 30 V, duration of 10 s, cathode of stainless steel.

Uniaxial bidirectional in-situ tensile tests were performed at room temperature (25±2 ℃) using a custom-developed mesoscopic mechanical test system (Fig. 2) with a constant crosshead speed of 0.2 mm/min. The experimental protocol employed a stepwise manual loading approach coupled with real-time microscopic observation. Before testing, the DIC system was calibrated by the inherent microstructural features of GH4169 superalloy as natural speckle patterns for strain field calculation[24]. High-resolution images of surface morphology were captured at incremental loading stages using a CCD camera (2048 pixel×2048 pixel). Grain rotation angles within the mesoscale region of 50 – 100 μm were quantified through custom-developed M-DIC software analysis. Complementary surface topography measurements were obtained using the New View 6200 white-light interferometric profilometer (Zygo) with 0.1 nm vertical resolution.

In-situ EBSD-tensile experiments were conducted on a JSM-7900F field emission scanning electron microscope (JEOL) integrated with Oxford Instruments Symmetry EBSD detector, Aztec Crystal automated orientation mapping system (v6.0), and Deben MT10578 micro-tensile stage. The experiment parameters are as follows: accelerating voltage of 20 kV, probe current of 18 nA, scan area of 1500 μm× 1600 μm, step size of 5 μm, and strain rate of 0.05 mm/min.

Fig. 3a shows the test points of specimen. The test protocol involved cyclic loading with intermittent holding: after each 0.5% strain increment, the load was stabilized for 15 min to acquire high-quality EBSD patterns. This process generated 23 discrete data points along the stress-strain curve (Fig. 3b), and orientation data processing was then performed using Aztec HKL Analysis Suite. Post-processing included noise reduction via neighbor pattern averaging and confidence index thresholding (>0.1).

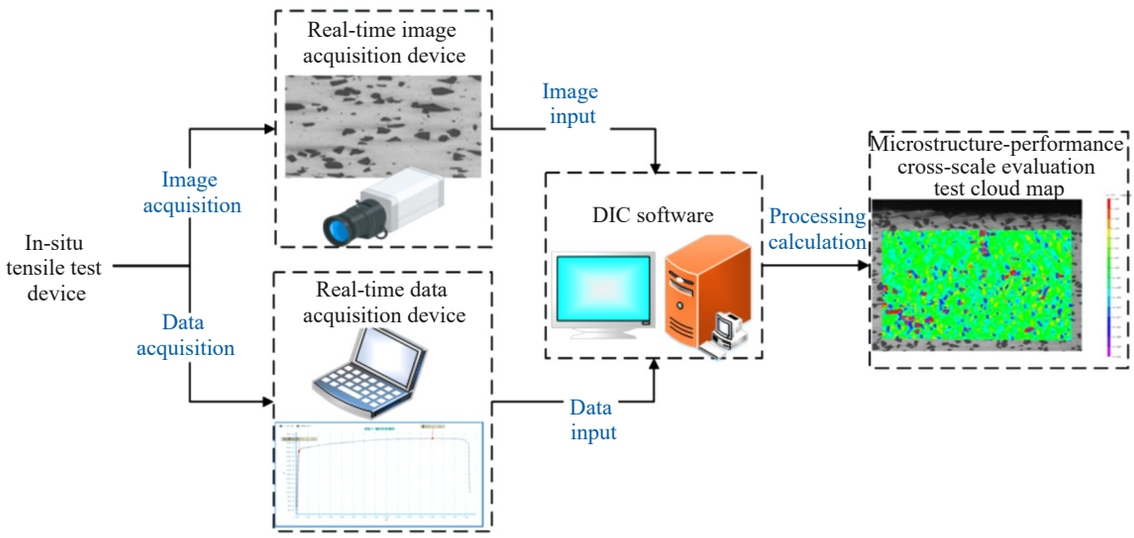

Fig.2 Schematic diagram of mesoscopic mechanical test system

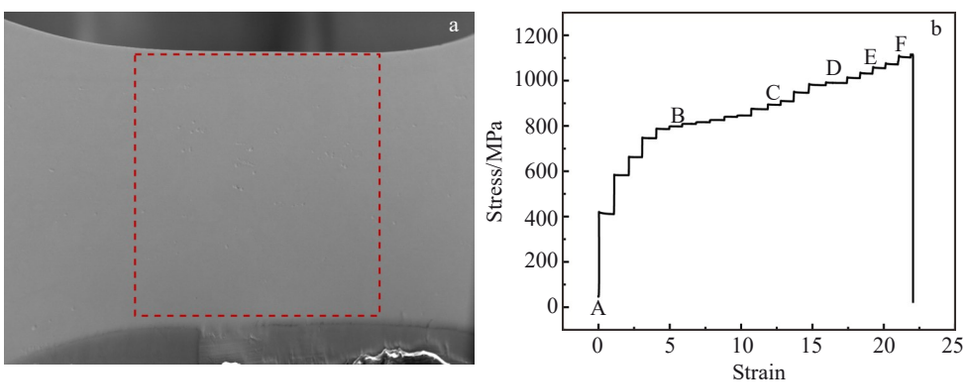

Fig.3 Schematic diagram of test points of specimen (a); strain-stress curve of in-situ EBSD-tensile test (b)

3 Results and Discussion

3.1 Grain rotation during tensile process

Fig. 4 shows the evolution of mesoscale microstructures under different stresses. The in-situ observation reveals three distinct deformation stages: elastic stage (Fig. 4a–4c), plastic deformation stage (Fig. 4d–4h), and fracture stage (Fig. 4i–4l). In the elastic stage, when the stress remains below 800 MPa, the polycrystalline structure maintains geometric stability with negligible grain shape variation, demonstrating typical Hookean behavior. In plastic deformation stage, beyond the yield point (>900 MPa), parallel slip bands emerge on grain surfaces. With the further increase in stress, slip band density exhibits positive correlation with stress magnitude, grains experience pronounced plastic distortion (ε>5%), and crystallographic rotation is initiated (θ<5°) through dislocation glide. In fracture stage, critical deformation occurs, including micropore nucleation at triple junctions, void coalescence forming microcrack nuclei, and crack propagation along high-angle grain boundaries.

The deformation heterogeneity manifests at two characteristic scales: intragranular and intergranular heterogeneities. Intragranular non-uniformity arises from activated slip systems $(12\bar{1})$ [111] and lattice rotation ($\Delta\theta \approx 2° - 8°$). Intergranular non-uniformity arises from strain incompatibility ($\Delta\varepsilon \approx 15\% - 20\%$) and grain boundary sliding ($\delta \approx 0.2–0.5$ μm).

This study quantifies rotation kinematics using DIC-based displacement field analysis (error<0.1 pixel) .

The initial image (stress=0 MPa) is taken as the reference image and the rectangular area marked in Fig. 4a was selected as the region of interest (ROI). DIC analysis was performed on each collected deformation map, and the results of calculation points in the selected ROI were analyzed. If the correlation coefficient is greater than 0.90, the calculation result of this point is credible and can be used for post-processing calculations. Then, the calculation results (displacement field and strain field) for all points within ROI were acquired. Thus, the characteristic boundary points of the grains within circle marked in Fig. 4a can be identified. Displacement parameters corresponding to points can be extracted to calculate the rotation angle of the grains of interest under different stresses or loads. The algorithm for calculating the rotation angle need to assume that the internal deformation of grain is minimal (ε<0.2%), or the intragranular deformation should be neglected. The circle area in Fig. 4a is

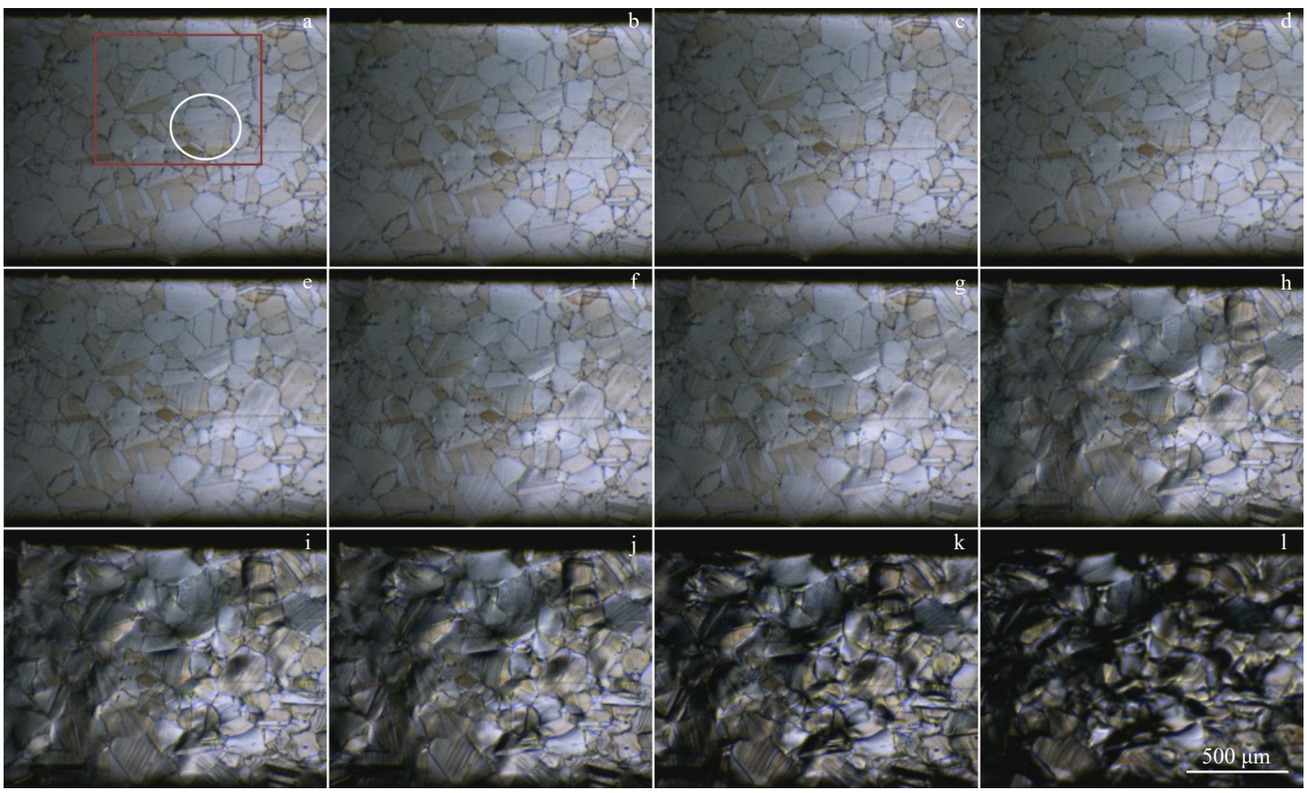

Fig.4 Evolution of mesoscale microstructures under different stresses: (a) 0 MPa, (b) 500 MPa, (c) 800 MPa, (d) 900 MPa, (e) 960 MPa, (f) 980 MPa, (g) 1000 MPa, (h) 1050 MPa, (i) 1080 MPa, (j) 1100 MPa, (k) 1150 MPa, and (l) 1200 MPa

selected for further analysis, and Fig. 5 shows its evolution under different stresses.

Assuming that the deformation field is a first-order deformation, the matrix can be constructed by the following steps. The computational framework employed polar decomposition to decouple rotational and deformational components through the following matrix operations.

$$\boldsymbol{M}_{XY} = (\boldsymbol{X}, \boldsymbol{Y}, 1), \boldsymbol{M}_{UV} = (\boldsymbol{U}, \boldsymbol{V}) \tag{1}$$

$$u = u_0 + u_x x + u_y y \tag{2}$$

$$v = v_0 + v_x x + v_y y \tag{3}$$

where $\boldsymbol{M}$ indicates the matrix; $\boldsymbol{X}$ and $\boldsymbol{Y}$ represent the spatial positions of grain boundary points; $\boldsymbol{U}$ and $\boldsymbol{V}$ denote the displacement vector components along the x-axis and y-axis, respectively; the subscripts XY and UV indicate the characteristics of matrix; x, y, u, and v are the specific values for coordinates $\boldsymbol{X}$, $\boldsymbol{Y}$, $\boldsymbol{U}$, and $\boldsymbol{V}$, respectively; the subscripts 0, x, and y indicate the initial state, along x-axis, and along y-axis, respectively.

The transformation matrix $\boldsymbol{f}$ satisfies the following relationships:

$$\boldsymbol{M}_{XY}\boldsymbol{f} = \boldsymbol{M}_{UV} \tag{4}$$

$$\boldsymbol{f} = \boldsymbol{M}_{XY}^{-1}\boldsymbol{M}_{UV} \tag{5}$$

As an overdetermined system, its matrix inverse is computed as the Moore-Penrose pseudo-inverse matrix through the least square minimization. The deformation gradient matrix $\boldsymbol{F}$, which maps reference configuration points to deformed configuration points, is derived from the transformation matrix $\boldsymbol{f}$ by:

$$\boldsymbol{F} = \boldsymbol{f}^{\mathrm{T}} + 1 \tag{6}$$

Applying singular value decomposition (SVD) to $\boldsymbol{F}$ yields:

$$\boldsymbol{F} = \boldsymbol{U}\Sigma\boldsymbol{V}^{\mathrm{T}} \tag{7}$$

Based on the orthogonal matrices $\boldsymbol{U}$ and $\boldsymbol{V}$ obtained via SVD, the pure rotation component $\boldsymbol{R}$ is determined as:

$$\boldsymbol{R} = \boldsymbol{U}\boldsymbol{V}^{\mathrm{T}} \tag{8}$$

The corresponding rotation angle θ is then calculated by:

$$\theta = \arcsin\left[\boldsymbol{R}(1, 0)\right] \tag{9}$$

Therefore, the displacement fields and rotation angles of grain 1 and grain 2 (marked in Fig. 5a) were quantitatively characterized, as shown in Fig.6 and Fig.7, respectively. Fig.6 shows the displacement fields of different displacement vector components under stress of 1000 MPa, revealing biaxial deformation components along x-axis and y-axis. The color bar is automatically generated by computational software, where negative value signs indicate directionality, and color variations represent changes in the displacement vector gradient. Superposition of the displacement vector components $\boldsymbol{U}$ and $\boldsymbol{V}$ indicates that the gradient variation of the displacement vector is the most significant along the 45° to x-axis, manifesting as maximum strain accumulation. This finding strongly aligns with the experiment result that the fracture plane is along 45° to stress direction in tensile tests.

As demonstrated in Fig. 7, the grain rotation behavior exhibits several characteristics: (1) progressive divergence in rotation angles/directions between adjacent grains with the

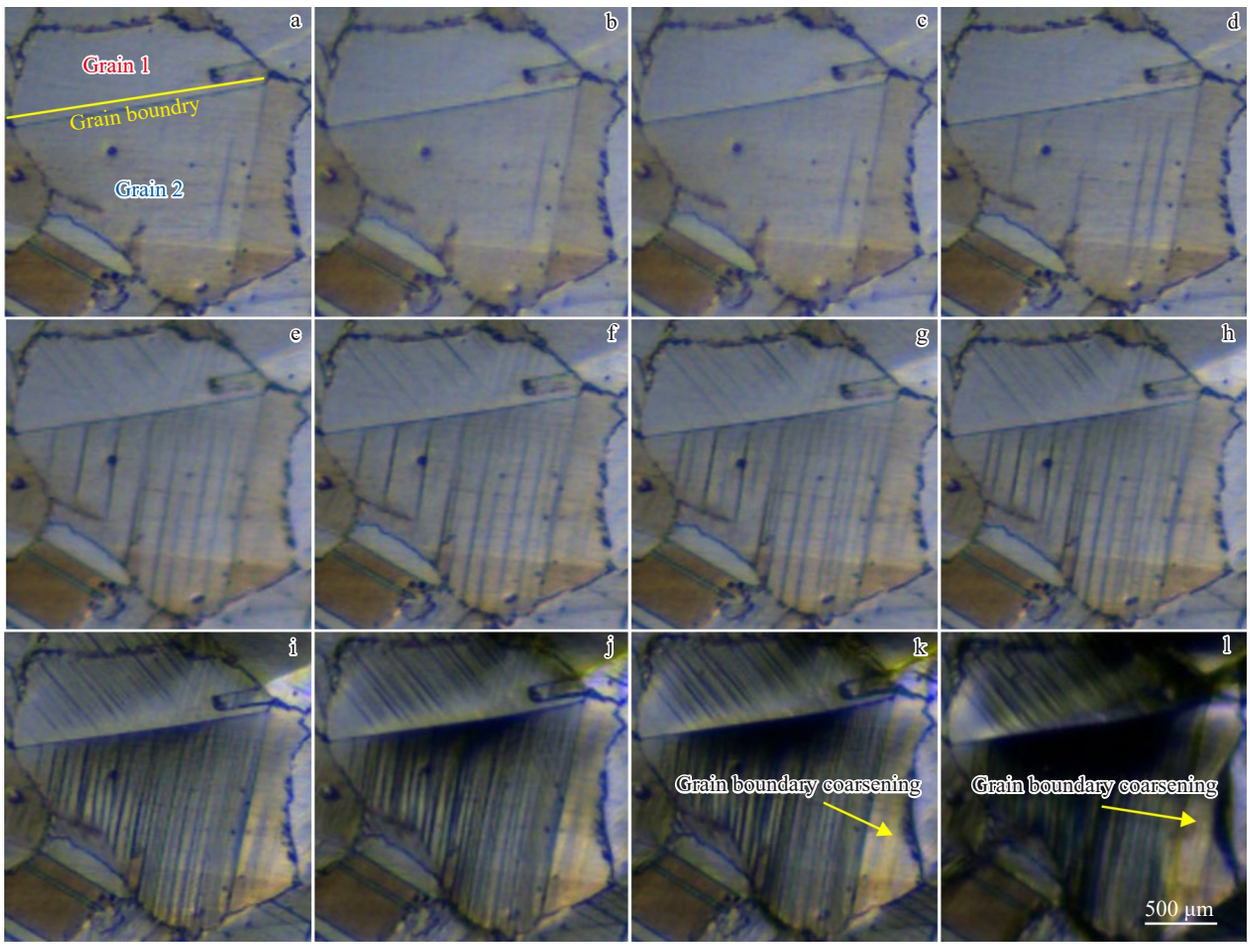

Fig.5 Evolution of grain 1 and grain 2 under different stresses: (a) 0 MPa, (b) 500 MPa, (c) 800 MPa, (d) 900 MPa, (e) 960 MPa, (f) 980 MPa, (g) 1000 MPa, (h) 1050 MPa, (i) 1080 MPa, (j) 1100 MPa, (k) 1150 MPa, and (l) 1200 MPa

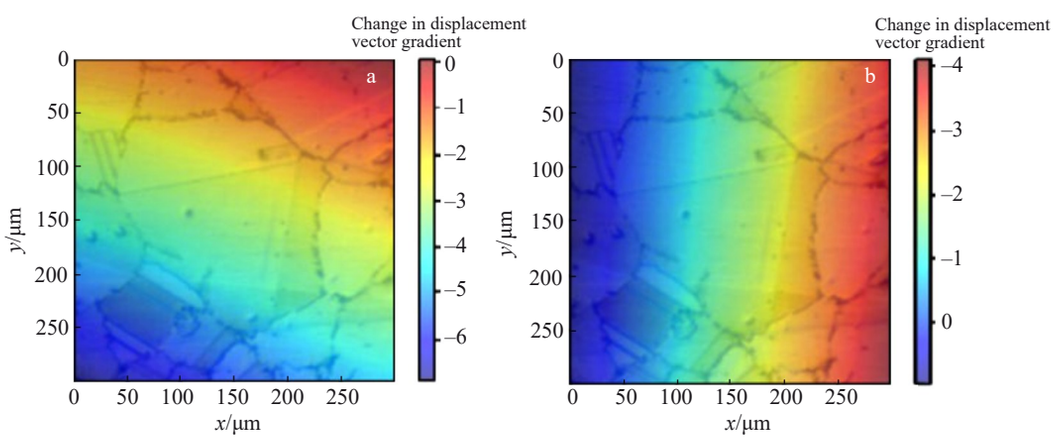

Fig.6 Displacement fields of displacement vector component $\boldsymbol{U}$ (a) and displacement vector component $\boldsymbol{V}$ (b) at plastic deformation stage

increase in stress; (2) oscillatory rotation pattern (alternating positive/negative rotations about the horizontal axis) rather than monotonic rotation (the rotation angle reaches about 0.6° under 1100 MPa). Microstructural evolution analysis shows that this stress level corresponds to significant grain boundary coarsening, micropore nucleation, and subsequent crack initiation, leading to final fracture, as shown in Fig. 5k (Stage I). These results demonstrate that the plastic deformation in polycrystalline materials involves coupled mechanisms of intragranular tensile deformation and intergranular rotation, which is particularly prominent in coarse-grained materials.

3.2 Surface coarsening phenomenon

Plastic deformation induces multiscale surface morphology evolution in polycrystalline materials, ranging from

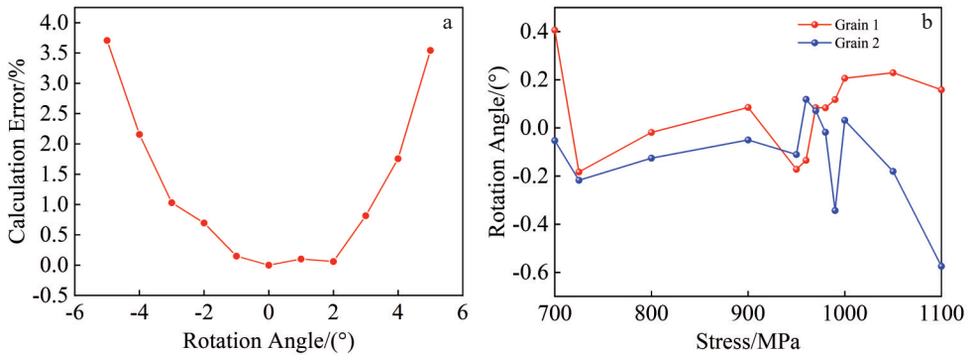

Fig.7 Calculation error of rotation angles of grain 1 and grain 2 calculated by DIC software (a); relationships between rotation angle and stress of grain 1 and grain 2 fitted by DIC software (b)

microscopic to macroscopic features. According to the results in Ref. [25], surface coarsening in polycrystalline metals manifests through three distinct scale regimes. (1) Microscale roughness (10^{-6}–10^{-4} m) originates from dislocation-mediated surface steps and forms characteristic surface undulations. (2) Mesoscale patterning (10^{-4}–10^{-3} m) emerges from particle aggregation and exhibits "orange peel" morphology[25–27]. (3) Macroscale topography (>10^{-3} m) results from cooperative grain cluster movement and develops ridge-valley structures[28–33].

Experimental verification was conducted via in-situ DIC tensile test at 1100 MPa (Stage III). Fig. 8 shows the optical 3D and 2D images of specimen after holding at 1100 MPa for 30 s. Wavy surface profile can be observed in slip zones with maximum height differential of 40 μm and preferred orientation at 45° to tensile axis. These observations confirm that the fracture stage corresponds to macroscale coarsening, the ridge-valley formation represents the final 3D morphological state before fracture, and the anisotropic deformation aligns with maximum shear stress theory.

Briefly, DIC analysis reveals significant bidirectional grain rotation during tensile deformation with rotation angles of ±0.6° under stress of 1100 MPa. The maximum displacement gradient is at 45° to the loading axis, which demonstrates strong coupling phenomena of grain boundary coarsening and micropore nucleation, confirming the shear-dominated deformation in local zones.

3.3 In-situ EBSD analysis of microstructural evolution

To investigate the microstructure evolution during tensile deformation, 6 characteristic points (points A – F in Fig. 3a) were selected for EBSD analysis. Fig. 9 presents a comprehensive characterization, including inverse pole figure (IPF), kernel average misorientation (KAM) maps, Schmid factor distributions, and (111) pole figures at different strain levels.

At the initial state (ε=0%), as shown in Fig. 9a, the microstructure consists of equiaxed grains with abundant annealing twins, and KAM analysis reveals the initial stress concentration at grain boundaries. At early deformation stage (ε=7%–14%), as shown in Fig. 9b–9c, IPF shows negligible grain morphology changes, and no visible slip lines can be observed. KAM results indicate that enhanced stress concentration occurs at grain boundaries, and Schmid factor analysis suggests that the activation of slip systems and dislocation accumulation initiates micropore formation at grain boundaries. At intermediate stage (ε=17.5%) as shown in Fig. 9d, clear grain deformation can be observed. Dislocations, restricted at the grain boundaries after gliding along grain interior slip systems, change the stress distribution

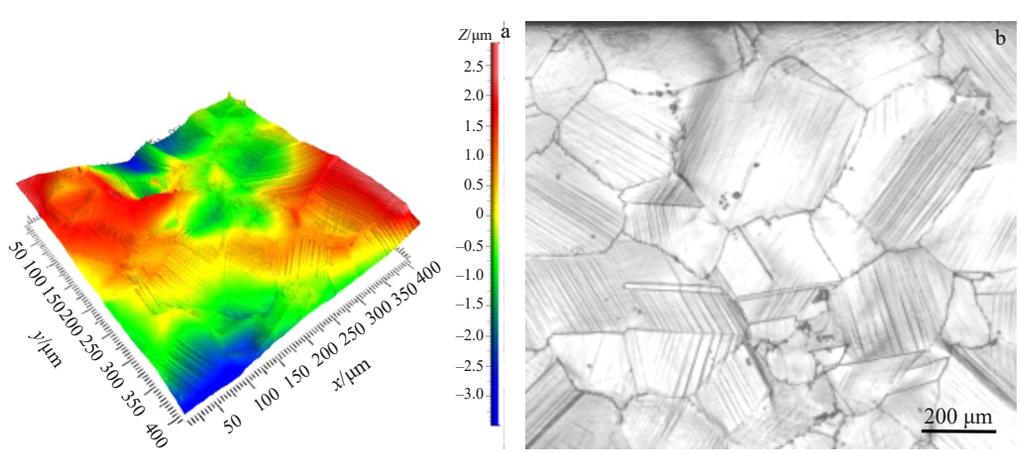

Fig.8 Optical 3D image (a) and 2D image (b) of specimen after holding at 1100 MPa for 30 s

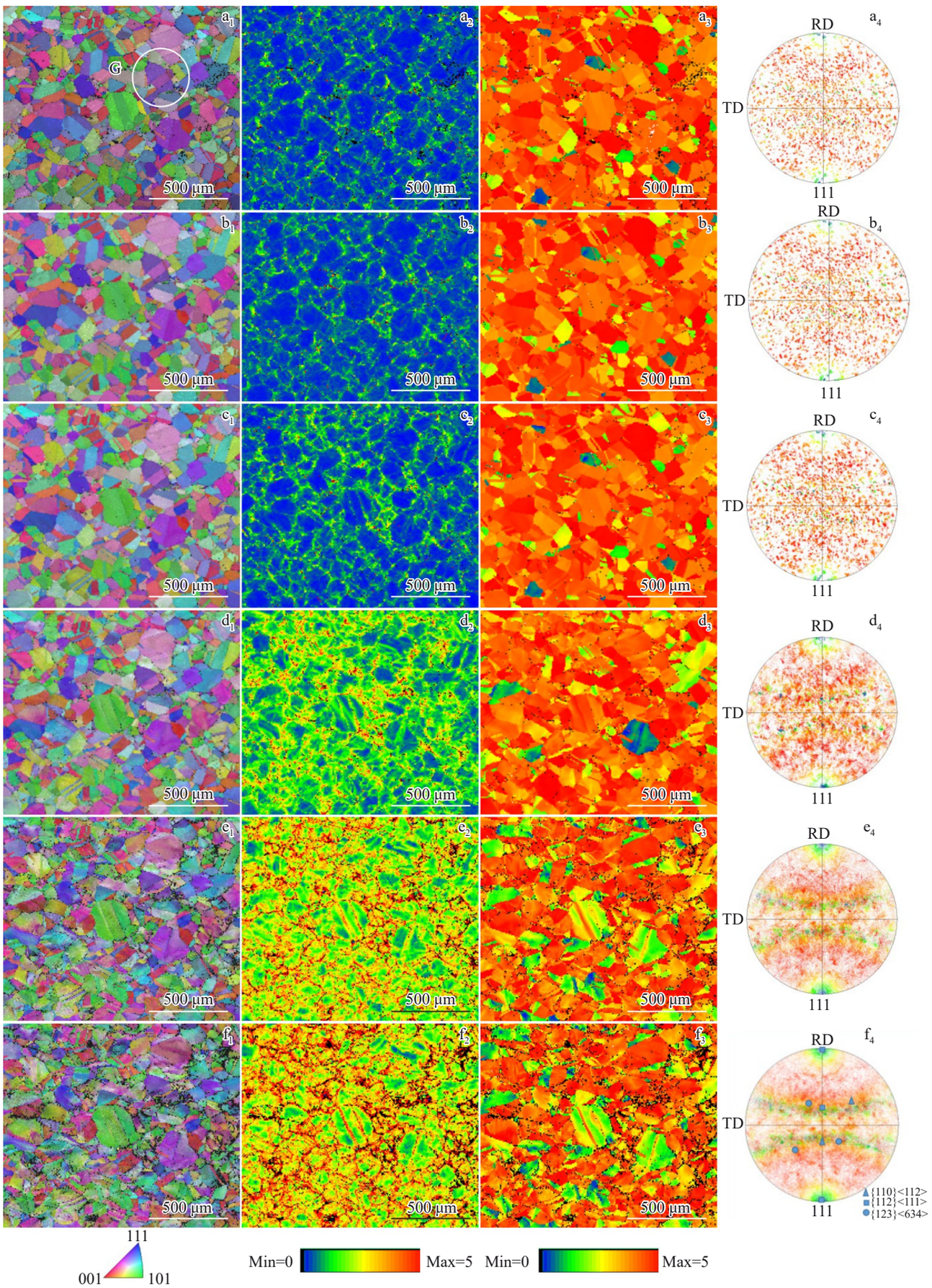

Fig.9 EBSD results of GH4169 superalloy under strain of 0% (a_1–a_4), 7% (b_1–b_4), 14% (c_1–c_4), 17.5% (d_1–d_4), 20% (e_1–e_4), and 22% (f_1–f_4): (a_1–f_1) IPFs; (a_2–f_2) KAM maps; (a_3–f_3) Schmid factor distributions; (a_4–f_4) (111) pole figures

pattern from concentration at the grain boundary to concentration within grains. This leads to microvoid coalescence at the grain boundary, resulting in microcrack formation and increasing intragranular damage. At final stage (ε=20%–22%), as shown in Fig. 9e–9f, distinct deformation occurs, presenting grain protrusions, torsional deformation, and well-developed slip bands. Maximum KAM values are detected at grain boundaries. Intragranular micropores are formed, indicating the imminent fracture. This progressive evolution demonstrates the transition from initial dislocation activity to final fracture through well-defined deformation stages.

With the increase in strain, a progressive development of parallel slip markings becomes evident on grain surfaces, exhibiting a strong correlation with the Schmid factor distribution. Crystallographic analysis reveals that the grains possessing higher Schmid factor (typically>0.4) demonstrate softer orientations. In accordance with Schmid law, these favorably oriented grains preferentially initiate slip deformation during the initial plastic stage, manifesting as distinct slip within grains.

The deformation process exhibits three key characteristics. (1) Slip system activation includes progressive activation of {111} <110> slip systems in soft-oriented grains, thereby increasing the slip trace density with strain. (2) Crystallographic rotation includes continuous lattice rotation from soft to hard orientations and dynamic evolution of Schmid factor distributions. (3) Texture development includes the formation of copper-type texture: C{112}<11$\bar{1}$> texture in hard-oriented grains, and S{123}<63$\bar{4}$> as well as B{110}<1$\bar{1}$0> components in soft-oriented grains. The contents of C{112}<11$\bar{1}$>, S{123}<63$\bar{4}$>, and B{110}<1$\bar{1}$0> textures are 32vol%, 28vol%, and 19vol%, respectively. The {111} pole figure analysis provides quantitative evidence of spatial distribution of soft/hard orientations, progressive texture evolution, and slip-induced rotation mechanisms.

This multiscale analysis demonstrates the fundamental relationship among crystallographic orientation, slip system activation, and texture development during plastic deformation. EBSD characterization analysis indicates a six-stage damage progression: (1) initiation of soft-oriented slip systems; (2) formation of intragranular parallel slip bands; (3) slip obstruction triggering dislocation multiplication; (4) strain energy accumulation at grain boundaries; (5) pore

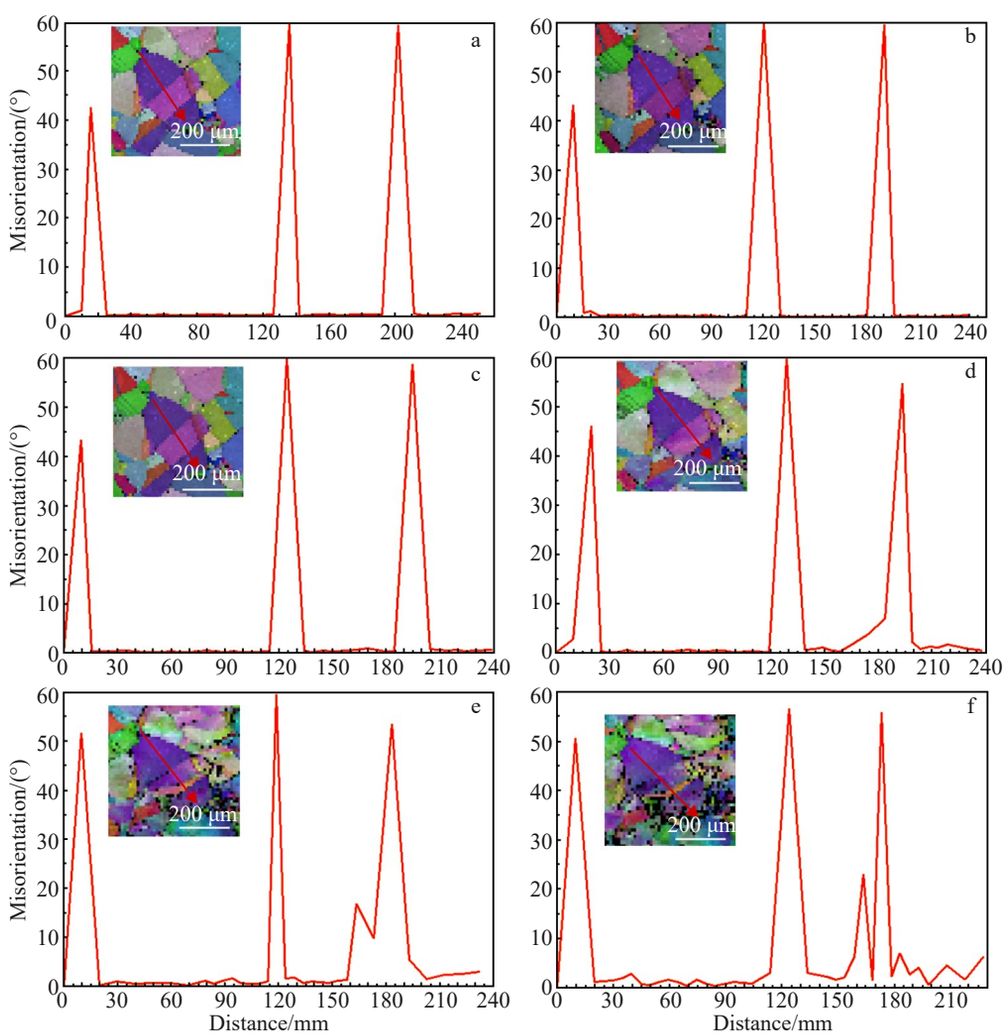

Fig.10 Evolution of misorientation of grain G marked in Fig.9a$_1$ under different strains: (a) 0%, (b) 7%, (c) 14%, (d) 17.5%, (e) 20%, and (f) 22%

nucleation at high-angle grain boundaries; (6) final crack initiation at stress-concentrated regions. Notably, coherent Σ3 twin boundaries exhibit 40% higher damage resistance than random high-angle grain boundaries.

The intragranular deformation exhibits significant heterogeneity during plastic deformation, which is primarily attributed to the non-uniform distribution of slip bands and crystallographic plane rotation within grains. In GH4169 superalloy, abundant annealing twins exist, and their boundaries have low coincidence-site-lattice value (ΣCSL). Normally, grain boundaries with low ΣCSL value play a crucial role in the plastic deformation behavior of alloy.

To investigate the deformation inhomogeneity and twin boundary orientation evolution, grain G marked in Fig. 9a$_1$ containing prominent twins (indicated by arrows in Fig. 10) was selected for misorientation analysis under different strains. Twin boundaries are identified by misorientation angles exceeding 40° . During the initial deformation stages (Fig. 10a – 10c), the misorientation angles exhibit minimal variation (<2°). When the strain reaches 17.5% (Fig. 10d), intragranular slip and grain rotation become pronounced. Incipient damage is initiated along twin boundaries, but microcracks have already developed at high-angle grain boundaries. Notably, the misorientation angle at twin boundary-adjacent regions increases to 15° at ε=20% (Fig. 10e), and it further exceeds 20° at ε=22% (Fig. 10f), demonstrating a progressive engulfment tendency of twin interfaces. These results reveal that the parallel slip bands sharing identical slip directions exhibit asynchronous activation and velocity disparities under stress. Besides, twin boundaries possess superior mechanical strength, compared with high-angle grain boundaries. These characteristics enable twin boundaries to effectively impede dislocation motion, consequently reducing creep rates and enhancing the mechanical performance of alloys.

4 Conclusions

1) The multiscale deformation mechanisms of GH4169 superalloy can be obtained by the in-situ tensile tests with DIC+EBSD method.

2) DIC analysis reveals significant bidirectional grain rotation during tensile deformation with rotation angles of ±0.6° under stress of 1100 MPa. The maximum displacement gradient is at 45° to the loading axis, which demonstrates strong coupling phenomena of grain boundary coarsening and micropore nucleation, confirming the shear-dominated deformation in local zones.

3) EBSD characterization analysis indicates a six-stage damage progression: (1) initiation of soft-oriented slip systems; (2) formation of intragranular parallel slip bands; (3) slip obstruction triggering dislocation multiplication; (4) strain energy accumulation at grain boundaries; (5) pore nucleation at high-angle grain boundaries; (6) final crack initiation at stress-concentrated regions. Notably, coherent Σ3 twin boundaries exhibit 40% higher damage resistance than random high-angle boundaries.

4) Texture analysis reveals that the room-temperature deformation produces copper-type textures: C{112} <11$\bar{1}$> (32vol%), S{123} <63$\bar{4}$> (28vol%), and B{110} <1$\bar{1}$0> (19vol%).

References

1 Zhang M, Ma C C, Xue C *et al*. *Rare Metal Materials and Engineering*[J], 2024, 53(8): 2131

2 Gaikwad S D, Vikram V D, Narayana M S N S *et al*. *Materials Science and Engineering A*[J], 2025, 943: 148744

3 Chen L L, Gao P, Luo R *et al*. *Rare Metal Materials and Engineering*[J], 2024, 53(7): 1882

4 Stinville J C, Lenthe W C, Miao J *et al*. *Acta Materialia*[J], 2016, 103(15): 461

5 Charpagne M A, Stinville J C, Callahan P G *et al*. *Materials Characterization*[J], 2020, 163(5): 110245

6 Deng H Z, Wang L, Liu Y *et al*. *Journal of Materials Research and Technology*[J], 2023, 23: 4747

7 Guan Y, Chen B, Zou J *et al*. *International Journal of Plasticity*[J], 2017, 88: 70

8 Xu Y, Zhang B, Yang Y *et al*. *Rare Metal Materials and Engineering*[J], 2023, 52(7): 2385

9 Lu G X, Wang Q, Attard B *et al*. *Transactions of Materials Research*[J], 2025, 1(3): 100039

10 Zhu Qifang, Sun Zongan, Shao Baohong *et al*. *Chinese Journal of Rare Metals*[J], 2007, 31(4): 451 (in Chinese)

11 Shen Z S, Huang Z Y, Wang J *et al*. *Engineering Failure Analysis*[J], 2025, 178(9): 109745

12 Zhao X, Zhang L C, Song Y D *et al*. *Materials Science and Engineering A*[J], 2023, 885: 145589

13 Gao W Q, Godfrey A. *Materials Letters*[J], 2022, 308: 131272

14 Hestroffer J M, Latypov M I, Stinville J C *et al*. *Acta Materialia*[J], 2022, 226: 117627

15 Nazari-Onlaghi S, Sadeghi A, Karimpour M *et al*. *Materials Science and Engineering A*[J], 2021, 812: 141107

16 Staroselsky A, Anand L. *International Journal of Plasticity*[J], 2003, 19(10): 1843

17 Wang J, Molina-Aldareguia J M, Llorca J. *Acta Materialia*[J], 2020, 188(15): 215

18 Akhtar A, Teghtsoonian E. *Acta Metallurgica*[J], 1969, 17(11): 1351

19 Nazari-Onlaghi S, Sadeghi A, Karimpour M. *Journal of Micromechanics and Microengineering*[J], 2021, 31(4): 1361

20 Hemery S, Villechaise P. *Acta Materialia*[J], 2019, 171(1): 261

21 Birosca S, Gioacchino D F, Stekovic S *et al*. *Acta Materialia*[J], 2014, 74(1): 110

22 Cappola J, Stinville J C, Charpagne M A *et al*. *Acta Materialia* [J], 2021, 204: 116492

23 Jin H, Lu W Y, Korellis J *et al*. *Journal of Strain Analysis for Engineering Design*[J], 2008, 43(8): 719

24 Nazari-Onlaghi S, Sadeghi A, Karimpour M. *Materials Science*

and Engineering A[J], 2022, 832: 142396
25 Sachtleber M, Raabe D, Weiland H. *Journal of Materials Processing Technology*[J], 2004, 148(1): 68
26 Lee P S, Piehler H R, Adams B L *et al*. *Journal of Materials Processing Technology*[J], 1998, 80–81(1): 315
27 Miranda-Medina M L, Somkuti P, Bianchi D *et al*. *Surface Engineering*[J], 2015, 31(7): 519
28 Kusters S, Seefeldt M, Van H P. *Materials Science and Engineering A*[J], 2010, 527(23): 6239
29 Panin A V, Romanova V A, Balokhonov R R *et al*. *Physical Mesomechanics*[J], 2012, 15(1–2): 94
30 Shin H J, An J K, Park S H *et al*. *Acta Materialia*[J], 2003, 51(16): 4693
31 Wouters O, Vellinga W P, Tijum V *et al*. *Acta Materialia*[J], 2006, 54(10): 2813
32 Wu P D, Lloyd D J. *Acta Materialia*[J], 2004, 52(7): 1785
33 Zhao Z, Radovitzky R, Cuitino A. *Acta Materialia*[J], 2004, 52(20): 5791

基于DIC与EBSD技术的GH4169合金拉伸变形行为实时研究

张丽民，张红菊，夏　雯，于丽敏，曹东东，贾荣光
(国标（北京）检验认证有限公司，北京 101400)

摘　要：通过同步介观数字图像相关（DIC）与电子背散射衍射（EBSD）原位表征技术，研究了GH4169高温合金在室温单轴拉伸下的变形行为。结果表明：在晶粒偏转动力学方面，基于自主研发M-DIC软件量化分析发现，在单轴拉伸时，沿拉伸轴水平方向呈双向旋转，在1100 MPa应力水平下，能够得到±0.6°的震荡偏转角，并在应力轴45°方向上萌生出晶界微孔。EBSD晶体学分析揭示了载荷依赖性滑移演变规律：在初始阶段，具有高施密德因子（>0.4）的软取向滑移系被激活，随后在滑移过程中转变为硬取向滑移系，在晶内形成平行滑移带，晶界出现位错塞积。单轴拉伸过程出现应变能累积特征，为双阶段积累模式：初期以晶界局部化为主，随后发展为晶内扩展，最终在大角度晶界处萌生裂纹，其中孪晶界展现出优于大角度晶界的力学稳定性。变形织构特征为铜型织构组分C｛112｝<11$\bar{1}$>、S｛123｝<63$\bar{4}$>和B｛110｝<1$\bar{1}$0>。完整变形链如下：软取向滑移系滑移→位错滑移启动→晶粒旋转主导应变分配→晶间应力集中→晶界开裂主导破坏。本研究揭示的跨尺度变形机制为晶界工程优化镍基高温合金提供了关键理论依据。

关键词：GH4169；原位拉伸；晶粒偏转；滑移；织构

作者简介：张丽民，女，1979年生，博士，高级工程师，国标（北京）检验认证有限公司，北京 101400，电话：010-82241376，E-mail：zhanglimin@gbtcgroup.com